

# High-Gain Traveling-Wave Parametric Amplifier Based on Three-Wave Mixing

Hampus Renberg Nilsson<sup>✉,\*</sup>, Anita Fadavi Roudsari<sup>✉</sup>, Daryoush Shiri<sup>✉</sup>, Per Delsing<sup>✉</sup>, and Vitaly Shumeiko<sup>✉</sup>

*Department of Microtechnology and Nanoscience - MC2, Chalmers University of Technology, Göteborg S-412 96, Sweden*

 (Received 18 May 2022; revised 29 November 2022; accepted 28 February 2023; published 19 April 2023)

We extend the theory for a Josephson-junction traveling-wave parametric amplifier (TWPA) operating in the three-wave-mixing regime and we propose a scheme for achieving high gain. The continuous three-mode model [P.K. Tien, *J. Appl. Phys.* **29**, 1347 (1958)] is, on one hand, extended to describe a discrete chain of Josephson junctions at high frequencies close to the spectral cutoff where there is no up-conversion. On the other hand, we also develop a continuous multimode theory for the small frequency limit where the frequency dispersion is close to linear. We find that in both cases the gain is significantly reduced compared to the prediction by the continuous three-mode model as the result of increasingly strong dispersion at the high frequencies and generation of up-converted modes at the small frequencies. The developed theory is in quantitative agreement with simulations of the full solution of the dynamical equations. To recover the high gain, we propose to engineer a chain with dispersive features to form a two-band frequency spectrum and to place the pump frequency within the upper band close to the spectral cutoff. We prove that there exists a sweet spot, where the signal and the pump are phase matched, while the up-conversion is inhibited. This results in a high gain, which grows exponentially with the length of the TWPA.

DOI: [10.1103/PhysRevApplied.19.044056](https://doi.org/10.1103/PhysRevApplied.19.044056)

## I. INTRODUCTION

Quantum limited parametric amplifiers [1] are useful tools for measuring and monitoring states of superconducting qubits. Built with nonlinear, superconducting lumped-element oscillators or transmission-line resonators and demonstrating high gain and small added noise [2–6], the parametric amplifiers became an essential part of the circuit quantum electrodynamics (cQED) [7] toolbox.

To build a large-scale multiqubit quantum processor, an optimization of qubit readout by multiplexing is desirable, which requires amplifiers with a large bandwidth, high gain and low added noise. Such a capability is provided by traveling-wave parametric amplifiers (TWPAs). During the last few years, the interest has rapidly grown in the development and investigation of the properties of different types of TWPAs.

The amplification principle of the TWPA is based on nonlinear interaction of a weak propagating signal with an

intense co-propagating wave (pump), which under a phase-matching condition results in an exponential spatial growth in the signal amplitude [8–10]. In the quantum regime, the TWPA is capable of generating signal squeezing and photon entanglement [11,12].

Within the cQED platform, two types of TWPAs are experimentally tested and theoretically studied: the first type uses the nonlinear kinetic inductance of a superconducting transmission line [13–20], and the second uses the nonlinear inductance of a chain of Josephson junctions [12,21–32]. The TWPAs are further distinguished depending on the type of nonlinear interaction they employ: three-wave mixing (3WM) or four-wave mixing (4WM).

The 3WM amplifiers employ the lowest order, cubic, nonlinearity of the inductive energy, which is similar to the  $\chi^{(2)}$  nonlinearity in optical crystals. Such nonlinearity is associated with the broken time-reversal symmetry, which can be introduced by applying a dc current bias, or a magnetic flux bias. The amplification occurs due to a down-conversion process, which is capable of providing an efficient amplification within a large bandwidth in a weakly dispersive medium already at relatively small pump intensity [10]. A useful property of this regime is the separation of the amplification band from the pump, and also the possibility of phase-preserving as well as phase-sensitive amplification.

\*Hampus.Renberg.Nilsson@chalmers.se

*Published by the American Physical Society under the terms of the [Creative Commons Attribution 4.0 International](https://creativecommons.org/licenses/by/4.0/) license. Further distribution of this work must maintain attribution to the author(s) and the published article's title, journal citation, and DOI. Funded by [Bibsam](https://www.bibsam.se/).*

In practice, however, the amplification performance of 3WM devices with weak frequency dispersion is compromised by the generation of pump harmonics [33] as well as signal and idler up-conversion [15,34,35].

The 4WM amplifiers employ the next order, quartic, nonlinearity of the inductive energy, which is similar to the  $\chi^{(3)}$  nonlinearity in optical fibers. Amplification in this regime is less efficient since it is a higher-order effect with respect to the pumping strength, and it also suffers from dephasing due to Kerr effect that makes exponential amplification impossible without dispersion engineering [23–25]. Furthermore, the pump position in the middle of the gain band is undesirable for certain applications.

In this paper, we theoretically investigate the efficiency of the TWPA operating in the 3WM regime, both for small and large frequencies. Our quest is to investigate whether it is possible to realize, in practice, full exponential amplification in a TWPA using 3WM by avoiding the poisoning effect of up-converted modes.

At first glance, the discreteness of the Josephson-junction chain allows solving the problem by placing the pump frequency close to the spectral cutoff, inherent in the discrete chains, and thus eliminating the up-converted modes [25]. Our analysis based on the exact solution for the discrete chain shows that this is, in principle, possible. However, to overcome the effect of dispersion, which becomes increasingly strong in the vicinity of the spectral cutoff, a rather strong pump signal is required that is unlikely to be realized in practice.

We propose to solve this difficulty by engineering a two-band frequency spectrum of the TWPA and placing the pump within the upper band close to the spectral cutoff. In this case, as we prove, there exists a sweet spot where the pump and the signal belong to the different bands and are exactly phase matched, while the generation of up-converted modes is inhibited since the pump is close enough to the cutoff. In the vicinity of this sweet spot, a rather broad window opens where a strong exponential amplification occurs. The width of this window is limited by the dispersion and up-conversion effects (cf. experimental observation in a kinetic inductance TWPA in Ref. [19]).

The structure of the paper is the following. In Sec. II we derive universal dynamic equations for three different kinds of TWPAs, that use either current-biased junctions, or magnetic-flux-biased radio-frequency superconducting quantum interference devices (rf SQUIDs) [29], or magnetic-flux-biased superconducting nonlinear asymmetric inductive elements (SNAILS) [31].

In Sec. III we derive the exact solution to the model containing only three modes involved in the down-conversion, while neglecting up-converted modes, and we evaluate the exponential gain and the frequency region where the exponential gain exists. This part is a generalization of the solution for a continuous medium in Ref. [10]. Here we

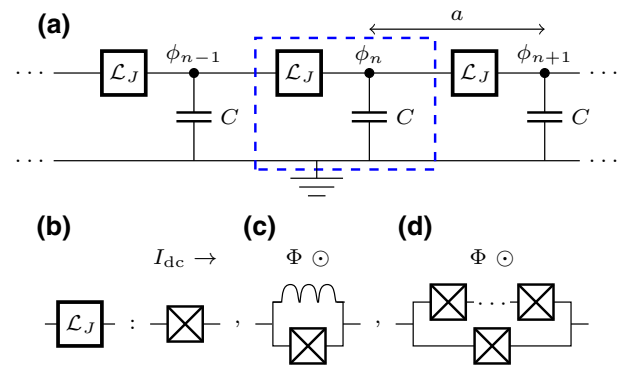


FIG. 1. Circuit diagram of a general discrete TWPA (a), the dashed line indicates a unit cell of length  $a$ . Options for the Josephson-junction block  $\mathcal{L}_J$ : (b) current-biased junction, (c) flux-biased rf SQUID, (d) flux-biased SNAIL.

also evaluate the pumping strength required for this model to be valid.

In Sec. IV we investigate the small frequency limit with weak frequency dispersion and show that generation of up-converted modes makes it impractically hard to achieve high exponential gain (cf. Ref. [34]). We also compare our theoretical results with simulations performed in Keysight PathWave Advanced Design System (ADS) and find a very good quantitative agreement.

In Sec. V we pursue the strategy of boosting the gain by engineering a two-band spectrum of the TWPA. We identify the sweet spots, where the high gain is achieved, for the two TWPA designs—adding resonators to unit cells [23–25], and periodically modulating the TWPA parameters [27]. The obtained results are summarized in Sec. VI.

## II. TWPA DYNAMICAL EQUATIONS

The traveling-wave parametric amplifier we study is a chain of identical cells, each consisting of a block of Josephson elements,  $\mathcal{L}_J$ , and a capacitor,  $C$ , as depicted in Fig. 1.

A convenient starting point for a dynamical description of the TWPA is the Lagrangian [36],

$$\mathcal{L} = \left(\frac{\Phi_0}{2\pi}\right)^2 \sum_{n=1}^N \left(\frac{C}{2} \dot{\phi}_n^2 + \mathcal{L}_J[\theta_n]\right), \quad (1)$$

where  $\phi_n(t)$  is the dynamical variable—the superconducting phase at node  $n$ ,  $\dot{\phi}_n(t)$  is its time derivative,  $\Phi_0 = h/(2e)$  is the magnetic flux quantum,  $\mathcal{L}_J$  is the Lagrangian of the Josephson-junction block, and  $\theta_n = \phi_n - \phi_{n-1}$  is the superconducting phase difference across the block.

We consider three flavors for the Josephson-junction blocks suitable for 3WM. The simplest one is the Josephson-junction block consisting of a single Josephson

junction, Fig. 1(b),

$$\mathcal{L}_J[\theta_n] = \left( \frac{C_J}{2} \dot{\theta}_n^2 + \frac{1}{L_J} \cos \theta_n \right), \quad (2)$$

where  $C_J$  and  $L_J = \hbar/(2eI_c)$  are the Josephson-junction capacitance and inductance, respectively.

In order to provide the 3WM mechanism, the Josephson junction has to be biased with a dc current,  $I_{dc}$ , which induces a constant shift of the phase difference across each cell,  $\theta_0$ , defined by equation,

$$\sin \theta_0 = \frac{I_{dc}}{I_c}. \quad (3)$$

After including this constant shift to the phase difference,  $\theta_n \rightarrow \theta_0 + \theta_n(t)$ , a dynamical equation for the TWPA is derived by varying the Lagrangian over the dynamical variable  $\phi_n(t)$  yielding,

$$\begin{aligned} \ddot{\phi}_n - \frac{C_J}{C} (\ddot{\theta}_{n+1} - \ddot{\theta}_n) - \bar{\omega}_0^2 (\sin \theta_{n+1} - \sin \theta_n) \\ - \bar{\omega}_0^2 \tan \theta_0 (\cos \theta_{n+1} - \cos \theta_n) = 0, \end{aligned} \quad (4)$$

where

$$\bar{\omega}_0^2 = \frac{\cos \theta_0}{L_J C} \quad (5)$$

is the resonance frequency of the current-biased  $L_J C$  oscillator.

The linear terms, with respect to  $\theta_n$ , in Eq. (4) define the spectral properties of propagating waves in the TWPA, while the nonlinear terms, with respect to  $\theta_n$ , are responsible for the mixing processes. In the absence of the biasing dc current, the 3WM term vanishes.

The TWPA dispersion relation is derived by assuming the solution to a linearized version of Eq. (4) as a discrete analog to the propagating wave with quasi-wave-vector  $\kappa$ ,  $\phi_n(t) \propto e^{i(\kappa n - \omega t)}$ , giving the relation,

$$2\bar{\omega}_0 \sin \frac{\kappa}{2} = \frac{\omega}{\sqrt{1 - (C_J/C)(\omega/\bar{\omega}_0)^2}}. \quad (6)$$

The dispersion relation has a cutoff at  $\kappa_c = \pi$ , where the frequency reaches the maximum value  $\omega_c$ ,

$$\omega_c = \frac{2\bar{\omega}_0}{\sqrt{1 + 4C_J/C}}. \quad (7)$$

The dispersion relation cutoff is related to the discrete nature of the TWPA, but it is also affected by the Josephson-junction capacitance. In practice, however, the latter is usually small,  $C_J \ll C$ , and we neglect it for most of the theoretical analysis throughout the paper, but keep it when comparing with simulations in Sec. IV C.

Assuming a small amplitude of the phase oscillation,  $|\theta_n| \ll 1$ , we expand trigonometric functions in Eq. (4) up to the second order, thus retaining the 3WM term but omitting the higher-order 4WM term, to get,

$$\ddot{\phi}_n - \bar{\omega}_0^2 (\theta_{n+1} - \theta_n) = -\frac{\bar{\omega}_0^2 \tan \theta_0}{2} (\theta_{n+1}^2 - \theta_n^2). \quad (8)$$

An alternative solution for a 3WM TWPA is to use a rf SQUID instead of a Josephson junction [29], as shown in Fig. 1(c). A rf SQUID includes an inductance  $L$  in parallel with the Josephson junction, which allows replacing the dc current bias with a dc magnetic flux bias to achieve 3WM. The Lagrangian  $\mathcal{L}_J$  in this case has the form

$$\mathcal{L}_J[\theta_n] = \left( \frac{1}{L_J} \cos(\theta_0 + \theta_n) - \frac{(\theta_0 + \theta_n + F)^2}{2L} \right), \quad (9)$$

where  $F = 2\pi \Phi / \Phi_0$  is the normalized magnetic flux. The dc phase shift  $\theta_0$  is now defined, in the absence of net dc current through the rf SQUID, by the relation

$$\frac{\sin \theta_0}{L_J} + \frac{\theta_0 + F}{L} = 0. \quad (10)$$

The dynamic equation now takes a form similar to the one in Eq. (8),

$$\begin{aligned} \ddot{\phi}_n - \omega_{\text{rf}}^2 (\theta_{n+1} - \theta_n) = -\frac{\bar{\omega}_0^2 \tan \theta_0}{2} (\theta_{n+1}^2 - \theta_n^2), \\ \omega_{\text{rf}}^2 = \left( \bar{\omega}_0^2 + \frac{1}{LC} \right). \end{aligned} \quad (11)$$

Another alternative design is to replace the rf SQUID with a SNAIL circuit [31], as shown in Fig. 1(d). This device can be viewed as a modification of a dc SQUID with several series connected junctions placed in one of the arms. The corresponding Lagrangian reads,

$$\mathcal{L}_J[\theta_n] = \frac{1}{L_{J1}} \cos(\theta_0 + \theta_n + F) + \frac{\mathcal{N}}{L_{J2}} \cos \frac{\theta_0 + \theta_n}{\mathcal{N}}, \quad (12)$$

here  $\mathcal{N}$  refers to the number of identical junctions in the top arm in Fig. 1(d). The biasing phase difference is defined in the absence of the net dc current through the SNAIL, by

$$\frac{2\pi}{\Phi_0} I_S = \frac{1}{L_{J1}} \sin(\theta_0 + F) + \frac{1}{L_{J2}} \sin \frac{\theta_0}{\mathcal{N}} = 0. \quad (13)$$

Proceeding with the derivation in a similar way to the single junction TWPA, we get the following dynamical

TABLE I. Summary of resonance frequencies and 3WM nonlinear coefficients for different TWPA designs.

TWPA	Bias	$\omega_0$	$\chi_3$
Junction	Current	$\bar{\omega}_0$ Eq. (5)	$\tan \theta_0$
rf SQUID	Flux	$\omega_{\text{rf}}$ Eq. (11)	$(\bar{\omega}_0/\omega_{\text{rf}})^2 \tan \theta_0$
SNAIL	Flux	$\omega_S$ Eq. (15)	Eq. (15)

equation for the SNAIL TWPA:

$$\ddot{\phi}_n - \omega_S^2(\theta_{n+1} - \theta_n) = -\frac{\omega_S^2 \chi_3}{2} (\theta_{n+1}^2 - \theta_n^2), \quad (14)$$

where

$$\omega_S^2 = \frac{1}{L_{J1}C} \cos(\theta_0 + F) + \frac{1}{L_{J2}CN} \cos \frac{\theta_0}{N},$$

$$\chi_3 = \frac{1}{\omega_S^2} \left( \frac{1}{L_{J1}C} \sin(\theta_0 + F) + \frac{1}{L_{J2}CN^2} \sin \frac{\theta_0}{N} \right). \quad (15)$$

It is worthwhile to note at this point that it is not possible to employ an asymmetric dc SQUID for three-wave mixing instead of the SNAIL: in this case  $N = 1$  in Eq. (15), and the nonlinear term in Eq. (14) turns to zero by virtue of Eq. (13).

Comparing Eqs. (4), (11), and (14), we find that they all have similar structures and can be written in a universal form:

$$\frac{1}{\omega_0^2} \ddot{\phi}_n - (\phi_{n+1} - 2\phi_n + \phi_{n-1}) = -\frac{\chi_3}{2} [(\phi_{n+1} - \phi_n)^2 - (\phi_n - \phi_{n-1})^2], \quad (16)$$

where  $\omega_0$  is the resonance frequency of the cell, and  $\chi_3$  is the 3WM nonlinear coefficient. Particular values of these quantities for different TWPA designs are presented in Table I.

### III. THREE-MODE MODEL

The amplification in a TWPA results from the process of resonant down-conversion, when the frequencies of three interacting waves, i.e., pump, signal, and idler, obey the resonance condition,  $\omega_p = \omega_s + \omega_i$ . Besides this process necessary for amplification, the nonlinear term in Eq. (16) generates a large set of up-converted modes of all the waves involved in the amplification and their combinations. These processes of up-conversion significantly degrade the performance of the amplifier, as we show in the next section.

To reveal the full amplification potential of the 3WM mechanism, we consider an ideal model where only three waves participating in the down-conversion are taken into account, while all the up-converted modes are neglected.

In this model, the field in the TWPA chain consists of a linear combination of three partial harmonic tones,

$$\phi_n(t) = \frac{1}{2} \sum_{\alpha=p,s,i} (A_{\alpha,n} e^{-i\omega_\alpha t} + \text{c.c.}) \quad (17)$$

whose amplitudes satisfy the equation that follows from Eq. (16):

$$\frac{\omega_\alpha^2}{\omega_0^2} A_{\alpha,n} + (A_{\alpha,n+1} - 2A_{\alpha,n} + A_{\alpha,n-1}) = \frac{\chi_3 \omega_\alpha}{2\pi} \int_0^{\frac{2\pi}{\omega_\alpha}} [(\phi_{n+1} - \phi_n)^2 - (\phi_n - \phi_{n-1})^2] e^{i\omega_\alpha t} dt, \quad (18)$$

where integration is done over the period of the corresponding mode.

For the pump amplitude, the right-hand side of Eq. (18) contains only the resonant products,  $A_{s,n}A_{i,n}$ , which are responsible for the pump depletion. For the amplifiers employed for qubit measurements, an input signal is typically approximately 1 nA, which is by 2 orders of magnitude smaller than the pump current, which is typically a considerable fraction of the critical current,  $I_c \sim 1 \mu\text{A}$ . Thus, for a power gain up to the order of 40 dB, the signal and idler remain weak compared to the pump within the whole TWPA chain,  $A_{s,n}, A_{i,n} \ll A_{p,n}$ , and we neglect their effect on the pump. As a result, Eq. (18) for the pump becomes linear and has a free propagating wave solution,  $A_{p,n} = A_p e^{-ik_p n}$ , with the dispersion relation,

$$\omega_p^2 = 4\omega_0^2 \sin^2 \frac{\kappa_p}{2}. \quad (19)$$

The dispersion relation has a cutoff at  $\omega_c = 2\omega_0$ ,  $\kappa_c = \pi$ , and is strongly dispersive in the vicinity of the cutoff. In the long-wave limit,  $\kappa_p \ll 1$ , the dispersion relation becomes linear,  $\omega_p \approx \omega_0 \kappa_p$ .

Proceeding to the equations for signal and idler we find that the only resonant contributions here come from the products  $A_{p,n}A_{i,n}^*$  for the signal, and  $A_{p,n}A_{s,n}^*$  for the idler. This implies that the equations form a linear equation set. The solution ansatz has the form,

$$A_{s,n} = A_s e^{i\frac{\kappa_p + \tilde{\kappa}}{2}n}, \quad A_{i,n}^* = A_i^* e^{-i\frac{\kappa_p - \tilde{\kappa}}{2}n}, \quad (20)$$

where  $\tilde{\kappa}$  is an unknown quasi-wave-vector. Then the corresponding equations in Eq. (18) reduce to an algebraic

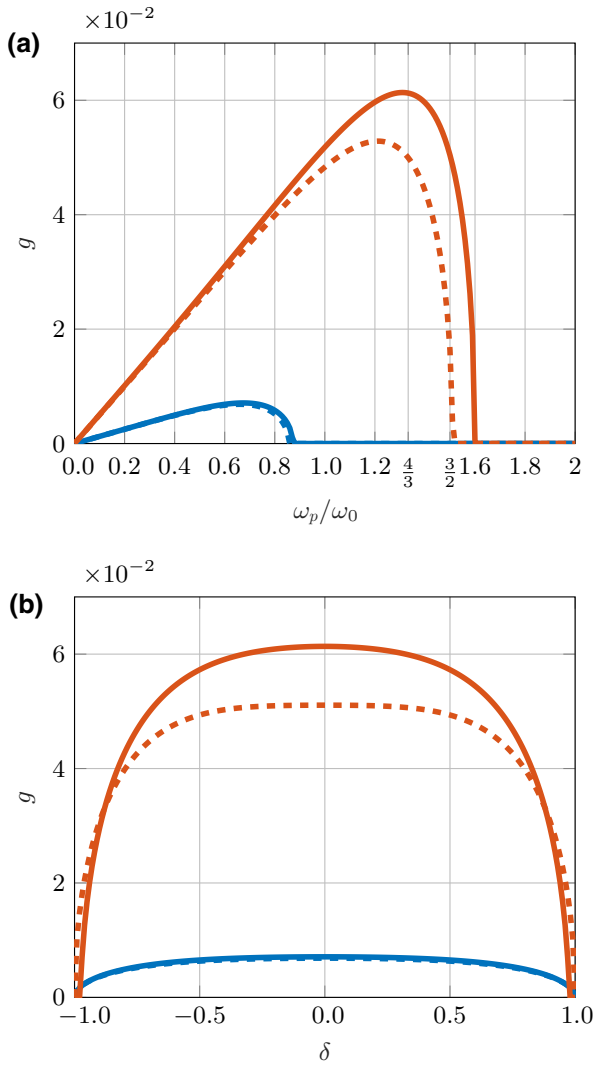


FIG. 2. Gain coefficient from numerically solving Eq. (22) (solid), and from Eq. (28) (dashed), for different pumping strengths,  $\varepsilon = 0.1$  (blue) and  $0.4$  (orange). (a) Gain coefficient at zero detuning,  $\delta = 0$ , as a function of pump frequency. (b) Gain coefficient as a function of detuning at the pump frequencies,  $\omega_p/\omega_0 = 0.67$  and  $1.31$ , corresponding to the maximum gain coefficient at zero detuning.

equation for spatiotemporally independent amplitude,  $A_s$ ,

$$\begin{aligned} \frac{\omega_s^2}{\omega_0^2} A_s - 4 \sin^2 \frac{\kappa_p + \tilde{\kappa}}{4} A_s \\ = -\frac{\chi_3 A_p}{2} \left[ (1 - e^{-i\kappa_p}) (1 - e^{i\kappa_p - \tilde{\kappa}/2}) \right. \\ \left. - (e^{i\kappa_p} - 1) (e^{-i\kappa_p - \tilde{\kappa}/2} - 1) \right] A_i^*, \end{aligned} \quad (21)$$

and a similar equation for  $A_i$  with the replacements,  $A_s \leftrightarrow A_i$ ,  $\omega_s \rightarrow \omega_i$ , and  $\kappa_p \rightarrow -\kappa_p$ .

The quasi-wave-vector  $\tilde{\kappa}$  is found from the solubility condition for Eq. (21) and equation for  $A_i$ , i.e., from the

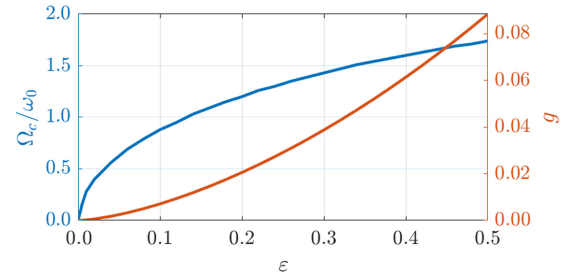


FIG. 3. Maximum value of the gain coefficient (orange) and the gain coefficient cutoff frequency  $\Omega_c$  (blue) as functions of the pumping strength.

condition for the determinant of the system to be equal to zero. After some algebra the corresponding equation can be presented in the form,

$$\begin{aligned} 0 = \sin \frac{\kappa_p - 2\kappa_s + \tilde{\kappa}}{4} \sin \frac{\kappa_p - 2\kappa_i - \tilde{\kappa}}{4} \\ \times \sin \frac{\kappa_p + 2\kappa_s + \tilde{\kappa}}{4} \sin \frac{\kappa_p + 2\kappa_i - \tilde{\kappa}}{4} \\ - \chi_3^2 |A_p|^2 \sin^2 \frac{\kappa_p}{2} \sin^2 \frac{\kappa_p + \tilde{\kappa}}{4} \sin^2 \frac{\kappa_p - \tilde{\kappa}}{4}. \end{aligned} \quad (22)$$

A solution to this equation generally has the imaginary part that describes the amplification effect. We quantify the amplification with the gain coefficient  $g = \text{Im}(\tilde{\kappa}/2)$ , which characterizes the amplitude gain per unit cell and is related to the power gain of TWPA as

$$G(\text{dB}) = 20gN \log_{10}(e), \quad (23)$$

where  $N$  is the number of unit cells.

The exact numerical solution for  $g$  at the degeneracy point,  $\omega_s = \omega_i = \omega_p/2$ , is presented in Fig. 2(a) for different pumping strengths. The pumping strength here is characterized through the quantity

$$\varepsilon = |\chi_3 \theta_p|, \quad \theta_p = 2 \sin \frac{\kappa_p}{2} A_p = \frac{\omega_p}{\omega_0} A_p. \quad (24)$$

Here  $\theta_p$  is the the amplitude of oscillation of phase difference across the cell associated with the pump amplitude at the node,  $A_p$ . At small frequencies,  $\omega_p \ll \omega_c$ ,  $\kappa_p \ll 1$ , the gain coefficient is small and grows linearly with frequency. It reaches a maximum and then sharply drops to zero at the gain cutoff frequency,  $\omega_p = \Omega_c$ . The maximum gain and  $\Omega_c$  depend on the pumping strength as illustrated in Fig. 3. As seen from Fig. 2(a), the maximum gain at large frequencies is quite large: for pumping strength  $\varepsilon \approx 0.4$ , the gain coefficient reaches the value  $g \approx 0.06$ , which translates to the power gain,  $G \approx 26$  dB, for a chain with  $N = 50$  cells.

A numerical solution of Eq. (22) for the gain coefficient as a function of detuning is presented in Fig. 2(b) with

solid lines. The plots are made for the pump-frequency values corresponding to maxima of the gain coefficients in Fig. 2(a) for the same pump intensities.

To better understand the gain properties, we derive an approximate analytical solution to Eq. (22). To this end we cast  $\tilde{\kappa}$  on the form,

$$\tilde{\kappa} = \kappa_s - \kappa_i - 2ig, \quad (25)$$

where quasi-wave-vectors,  $\kappa_{s,i}$ , are related to the signal and idler respective frequencies via the dispersion relation similar to Eq. (19). We also define the detuning from the degeneracy point,

$$\delta = \frac{\omega_s - \omega_p/2}{\omega_p/2}, \quad (26)$$

and the phase mismatch  $\Delta(\delta)$ ,

$$\Delta(\delta) = \kappa_p - \kappa_s(\delta) - \kappa_i(\delta). \quad (27)$$

At weak coupling,  $\varepsilon \ll 1$ , the gain coefficient is small, as is also seen in Fig. 2(a), in comparison with the wave vectors  $\kappa_p \sim \kappa_s \sim \kappa_i$ , which are of order unity at high frequencies, as given by the dispersion relation in Eq. (6). On the other hand, the phase mismatch, which is sufficient to suppress the gain is also small. Therefore, both  $g$  and  $\Delta(\delta)$  are small additive corrections to  $\kappa_{p,s,i}$ , and can be omitted from the corresponding terms in Eq. (22). This approximation yields the explicit solution for  $g$ ,

$$\begin{aligned} \sinh^2 \frac{g}{2} = & -\sin^2 \frac{\Delta(\delta)}{4} + \chi_3^2 |A_p|^2 \frac{\sin^2 \frac{\kappa_p}{2}}{\sin \kappa_s \sin \kappa_i} \\ & \times \left( \sin^2 \frac{\kappa_s + \kappa_i}{4} - \sin^2 \frac{\kappa_s - \kappa_i}{4} \right)^2. \end{aligned} \quad (28)$$

The obtained solution is a generalization to a discrete chain and arbitrary frequency of the result obtained in Ref. [10] for a continuous medium. One can see from Eq. (28) that it is the competition between the nonlinear coupling controlled by the intensity of the pump (the second term on the right) and the phase mismatch (the first term on the right) that determines whether  $g$  is real or imaginary, i.e., whether exponential amplification occurs or not. The sharp drop of the gain is explained by the increasingly strong dispersion near the cutoff frequency. At zero detuning, Eq. (28) reduces to the form

$$\sinh^2 \frac{g}{2} = -\sin^2 \frac{\Delta}{4} + \chi_3^2 |A_p|^2 \sin^4 \frac{\kappa_p}{4}, \quad (29)$$

where

$$\Delta = \Delta(0) = \kappa_p - 2\kappa_s, \quad (30)$$

is the phase mismatch between the frequency points,  $\omega_p$  and  $\omega_p/2$ . This solution is represented in Fig. 2 with dashed lines.

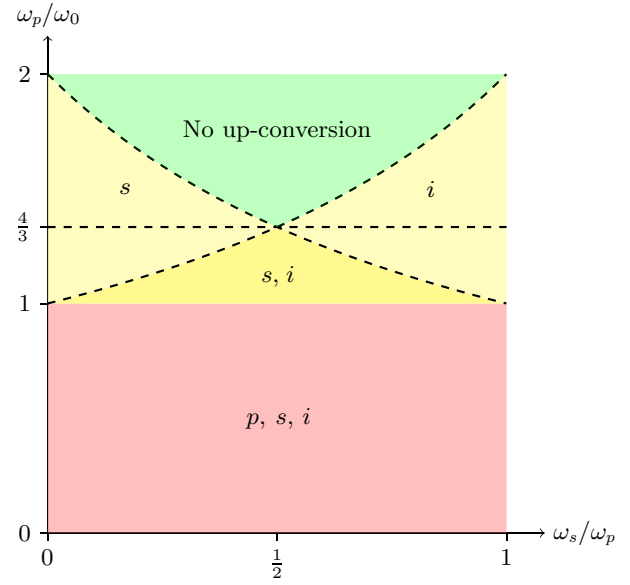


FIG. 4. Regions of the absence and presence of up-conversion of pump, signal, and idler. In the green region no up-conversion takes place, horizontal dashed line indicates  $\Omega_{\text{th}}$ ; in the light yellow regions, up-conversion of either signal or idler is possible, while in the yellow region both signal and idler are up-converted but pump is not; in the pink region all three modes are up-converted.

Equation (22) and its approximate analytical solution, Eq. (28), together with numerical solution presented in Fig. 2 constitute the first main result of this paper.

### A. Validity of the model

The validity of the model above relies on the absence of up-converted modes of the pump, signal, and idler. For the pump, the condition,  $\omega_p > \omega_0$ , guarantees that the second pump harmonic falls above the cutoff,  $\omega_c = 2\omega_0$ . For the signal and idler the lowest bound is established by condition that the up-converted signal at zero detuning falls above the cutoff,  $\omega_p/2 + \omega_p > 2\omega_0$ . This yields a more stringent constraint,  $\omega_p > \Omega_{\text{th}} = 4\omega_0/3$ . At pump frequency larger than this threshold value, the detuned signal and idler are not up-converted within the band defined by equation,

$$|\delta| < 3 \left( 1 - \frac{\Omega_{\text{th}}}{\omega_p} \right). \quad (31)$$

This situation is illustrated in Fig. 4.

Therefore, we conclude that the three-mode model considered is justified, when the gain cutoff frequency exceeds the threshold for no up-conversion,  $\Omega_c(\varepsilon) > \Omega_{\text{th}}$ , and within the bandwidth in Eq. (31). This condition imposes the lowest bound for the required pumping strength. An accurate estimate of the lowest bound is extracted from the

numerical solution to Eq. (22),

$$\varepsilon \gtrsim 0.25. \quad (32)$$

To obtain an analytical estimate we assume,  $g = 0$  in Eq. (29), to get,

$$\chi_3 |A_p| > \frac{\sin \frac{\Delta}{4}}{\sin^2 \frac{\kappa_p}{4}}. \quad (33)$$

At  $\omega_p = \Omega_{\text{th}}$ ,  $\kappa_p \approx 0.46\pi$ , and for zero detuning,  $\delta = 0$ , we have  $\kappa_s \approx 0.22\pi$ , giving  $\Delta \approx 0.03\pi$ . This results in the bound for the pumping strength,  $\chi_3 |A_p| > 0.20$ , or  $\varepsilon \gtrsim 0.27$ , which slightly overestimates the exact result from Eq. (32).

The crucial question is now whether the required coupling strength can be experimentally achieved with a feasible pump intensity. Let us first consider the dc current-biased TWPA. The pumping strength here is limited by the switching of the Josephson junctions to the resistive branch. In the quantum limit, the maximum dc supercurrent that the junction can sustain corresponds to the disappearance of the last quantized energy level from the well of the tilted Josephson potential. The maximum dc supercurrent can be crudely estimated from the relation,  $\hbar\omega_{\text{pl}}/2 \sim \Delta U$ , where  $\omega_{\text{pl}} = \sqrt{\cos \theta_0 / (L_J C_\Sigma)}$  is the effective plasma frequency for the junction,  $C_\Sigma = C/2 + C_J \approx C/2$ , and  $\Delta U \approx (2E_J/3) \cos^3 \theta_0$  is the depth of the well of the tilted Josephson potential. Impedance matching of the TWPA with the transmission line,  $\sqrt{L_J / (C \cos \theta_0)} = Z_0$ , gives for the maximum current,  $\cos^2 \theta_0 \sim 3\pi \sqrt{2Z_0/R_q}$ , where  $R_q = h/(2e^2)$  is the quantum resistance; this corresponds to  $I_{\text{dc}} \sim 0.97I_c$ . Assuming that the quasiclassical tunneling rate,  $\Gamma \propto \exp(-7.2\Delta U/\hbar\omega_{\text{pl}})$  [37], is valid for the two-three quantized energy levels in the well [38], and also taking into account the experimental observations, e.g., in Ref. [39], we may safely assume for the switching current value,  $I \approx 0.9I_c$ .

When the pump is on and has a small frequency,  $\omega_p \ll \omega_{\text{pl}}$ , the instant adiabatic current consists of the dc biasing current,  $I_{\text{dc}}$ , and the pump ac current,  $I_p$ , and their sum should not exceed the switching current,  $I_{\text{dc}} + I_p < 0.9I_c$ . The maximum pumping strength under this constraint is,  $\varepsilon = 0.28$ , which is achieved at  $I_{\text{dc}} = 0.63I_c$  and  $I_p = 0.27I_c$ . Although this pumping strength is above the bound in Eq. (32), the frequency window where the model is valid is very small,  $\Omega_c - \Omega_{\text{th}} \approx 0.06\omega_0$ , Fig. 4, making the amplification bandwidth unacceptably narrow. Furthermore, the corresponding pumping current is too large given the theory constraint,  $I_p \ll I_c$ , more feasible would be the lower current values,  $I_p \sim 0.1I_c$ . In addition, a spread of the junction parameters in a real TWPA would also reduce the estimated pumping strength.

What is more, however, is that the relevant ac regime is nonadiabatic: the pump frequencies above the no-up-conversion threshold,  $\omega_p > \Omega_{\text{th}} \approx 1.33\bar{\omega}_0$ , are close to and even higher than the plasma frequency,  $\omega_{\text{pl}} = \sqrt{2}\bar{\omega}_0 \approx 1.41\bar{\omega}_0$ . In this regime, the resonant excitation facilitates tunneling (especially due to the multiphoton processes at large pump amplitude), therefore the biasing current should be even smaller than in the adiabatic regime, hence the pumping strength would be further reduced.

In the case of a rf SQUID TWPA, the maximum nonlinear coupling is achieved at  $\theta_0 = \pi/2$  [29], when  $\chi_3 = L/L_J$ . For a nonhysteretic regime,  $L/L_J < 1$ , combination of this constraint with a small value of the amplitude of phase oscillation,  $\theta_p < 0.1$ , results in a pumping strength,  $\varepsilon < 0.1$ , which is below the threshold, Eq. (32). A similar argument also applies to the SNAIL TWPA.

To summarize, we conclude that the three-mode amplification regime, which would provide the high exponential gain at high frequencies,  $\omega_p \sim \omega_0$  cannot be realized in practice with any of the TWPA designs considered here. The desired condition,  $\Omega_c(\varepsilon) > \Omega_{\text{th}}$ , cannot be fulfilled because of small values of nonlinear 3WM coefficients in realistic devices and limited pumping current.

To go beyond the studied three-mode model, two strategies can be followed. One is to consider the lower frequencies and include the up-converted modes in the model, while the other is to keep the three-mode model but consider dispersion engineering at high frequencies. In the next section we discuss the first option in detail.

#### IV. QUASILINEAR DISPERSION REGIME

In this section we analyze TWPA performance in the small frequency limit,  $\omega \ll \omega_0$ ,  $\kappa \ll \pi$ , where the dispersion relation is quasilinear. In this limit, higher-order nonlinear dispersive effects and the effect of a cutoff frequency are neglected. The limit of the continuous medium is natural for the kinetic inductance TWPA, but it is also considered in most of publications devoted to the Josephson-junction TWPAs.

In this limit the discrete chain of the Josephson junctions is described with a continuous variable,  $an \rightarrow x$ ,  $\phi_n \rightarrow \phi(x)$ , where  $a$  is the physical length of the unit cell. Then the difference equation, Eq. (16), turns into a differential equation,

$$\begin{aligned} & \frac{1}{\omega_0^2} \ddot{\phi} + 4 \sin^2 \frac{a\hat{k}}{2} \phi \\ & = \frac{\chi_3}{2} \left\{ \left[ (1 - e^{-ia\hat{k}}) \phi \right]^2 - \left[ (e^{ia\hat{k}} - 1) \phi \right]^2 \right\}, \quad (34) \end{aligned}$$

where  $\hat{k} = -i\partial_x$ . Keeping the lowest-order terms with respect to  $a$  in the expansion of the interaction term, we

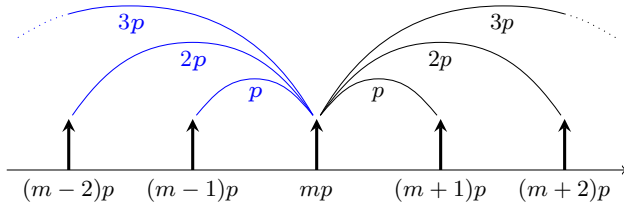


FIG. 5. Interaction of  $m$ th pump harmonic illustrating structure of Eq. (37). Each process is marked with the pump harmonic that is driving the process.

write Eq. (34) in the form,

$$\frac{1}{\omega_0^2} \ddot{\phi} + 4 \sin^2 \frac{a\hat{k}}{2} \phi = \frac{\chi_3 a^3}{2} i\hat{k} (\hat{k}\phi)^2. \quad (35)$$

This dynamical equation (and a similar one for the 4WM) is a standard object of study in the TWPA literature.

To analyze the resonant wave dynamics described by this equation one has to take into account, in addition to the down-conversion discussed in the previous section, the processes that are efficient for a weakly dispersive medium: (i) generation of pump harmonics with frequencies  $n\omega_p$  [33], (ii) up-conversion of the signal and down-converted idler by the pump tone and its harmonics,  $\omega_{s,i} + n\omega_p$  [34]. The processes that can be neglected for a weak signal include pump depletion and generation of signal and idler harmonics and their intermodulation products.

### A. Pump harmonics

Let us first consider pump harmonic generation. When a pump tone is injected, the field in the cavity has the form

$$\phi(x, t) = \frac{1}{2} \sum_{m=1}^M (A_{mp}(x) e^{i(k_{mp}x - m\omega_p t)} + \text{c.c.}), \quad (36)$$

where  $k$  is a wave vector related to  $\omega$  via the free wave dispersion relation,  $ka = 2 \arcsin(\omega/(2\omega_0))$ , and  $M$  is the number of harmonics included in the computation (see below). A slow variation of the amplitudes of the harmonics accounts for the effect of nonlinear interaction.

Substituting Eq. (36) in Eq. (35) we get a set of  $M$  coupled nonlinear equations for the pump harmonics,

$$A'_{mp} = \frac{\chi_3 a}{4} \times \left( \sum_{n=m+1}^M k_{np} k_{(n-m)p} A_{np} A_{(n-m)p}^* e^{i\Delta_{n,m} x} - \frac{1}{2} \sum_{n=1}^{m-1} k_{np} k_{(m-n)p} A_{np} A_{(m-n)p} e^{-i\Delta_{m,n} x} \right), \quad (37)$$

where the prime signifies spatial derivative,  $A' = dA/dx$ ,  $\Delta_{n,m} = k_{np} - k_{mp} - k_{(n-m)p}$ , and  $m \in \{1, \dots, M\}$  is the harmonic number. In this equation, the first sum describes coupling to the higher harmonics, while the second sum describes coupling to the lower harmonics, as illustrated in Fig. 5. The factor  $1/2$  in the second sum accounts for the double counting in the sum, e.g.,  $n = 1$  and  $n = m - 1$ .

When the number of harmonics is restricted to  $M = 2$ , an analytical solution is available [33], which shows that for a linear dispersion the injected tone is fully converted to the second harmonic on a length inversely proportional to the amplitude of the injected signal. In the presence of dispersion, both harmonics exhibit oscillatory behavior (see blue curve in Fig. 7) while preserving the quantity  $|A_p(x)|^2 + 4|A_{2p}(x)|^2 = \text{constant}$ . Analytical solutions are also available for a larger number of harmonics, but their behavior becomes rather complex, so we resort to numerics.

We perform a numerical study under the assumption that all relevant harmonics have frequencies well below the cutoff. For a weak dispersion the pre-exponential factors in Eq. (37) can be approximated with linear functions,  $k_{mp}a = m\omega_p/\omega_0$ , while the exponential dephasing factors are approximated with the lowest-order (cubic) corrections. The latter can be expressed through the dephasing  $\Delta \approx k_p^3 a^2/32$  defined in Eq. (30),

$$\Delta_{m,n} = 8\Delta d_{m,n} = \frac{k_p^3 a^2}{4} d_{m,n}, \quad d_{m,n} = \frac{1}{2} mn(m-n). \quad (38)$$

To compute and analyze the solutions to Eq. (37), it is convenient to introduce dimensionless spatial coordinate and rescaled harmonic amplitudes,

$$\xi = \frac{\varepsilon k_p}{4} x, \quad a_{mp}(\xi(x)) = m \frac{A_{mp}(x)}{A_p(0)}, \quad (39)$$

where  $\varepsilon$  is the pumping strength defined in Eq. (24), which has the form in the small frequency limit,  $\varepsilon = |\chi_3 A_p(0)| k_p a$ . Then Eq. (37) reduces to a compact form,

$$(a_m)'_{\xi} = m \sum_{n=m+1}^M a_n a_{n-m}^* e^{i\mu \xi d_{n,m}} - \frac{m}{2} \sum_{n=1}^{m-1} a_n a_{m-n} e^{-i\mu \xi d_{m,n}}, \quad (40)$$

where the spatial behavior of all harmonics is described with a *single scaling parameter*,

$$\mu = \frac{32\Delta}{\varepsilon k_p} \approx \frac{k_p^2 a^2}{\varepsilon}. \quad (41)$$

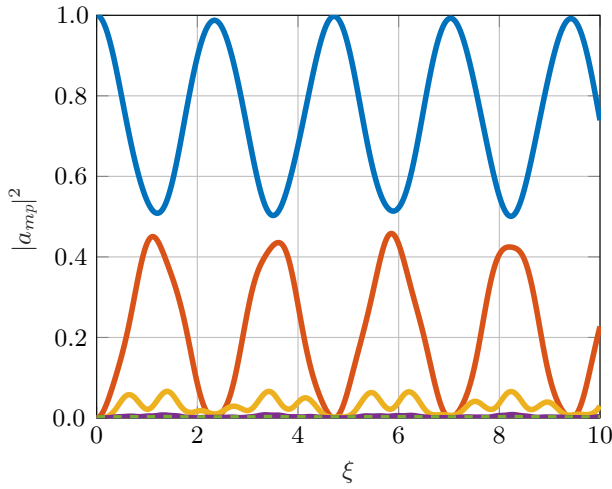


FIG. 6. First five harmonics for  $\mu = 2$  and  $M = 5$ : first (blue), second (orange), third (yellow), fourth (purple), and fifth (dashed green).

This parameter is proportional to the ratio of the dephasing and the nonlinear pumping strength, and has clear physical meaning indicating that it is the interplay between the dispersion and the nonlinear coupling (the pumping strength) that defines the behavior of the harmonics.

The differential equations in Eq. (40) are solved numerically for different values of  $\mu$  and  $M$  using fourth and fifth order Runge-Kutta methods of the MATLAB function `ode45`.

The spatial dependence of the solutions truncated at  $M = 5$  is shown in Fig. 6 for  $\mu = 2$ . All the harmonics oscillate but while amplitudes of the first and second harmonics are substantial, the amplitudes of higher harmonics,  $m = 3, 4, 5$ , are decreasingly small. Correspondingly, the effect of the latter on the main pump tone is small, as illustrated in Fig. 7 for  $\mu = 2$  and different values of  $M$ . Here the solution for the main pump tone coupled to three harmonics clearly differs from the one coupled to two harmonics, but the more harmonics are included the smaller effect they have on the solution for the main pump tone. The solution for the main pump tone appears to converge at  $M \gtrsim 5$ .

Our numerical studies show that the number of large-amplitude harmonics depends on the value of  $\mu$ , the number of large-amplitude harmonics increases when  $\mu$  decreases, which corresponds to a weaker dispersion or stronger pumping. Furthermore, for a given  $\mu$ , the amplitudes of harmonics with numbers exceeding a certain critical value,  $m > M_c$ , become negligible on a given length, as illustrated in Fig. 8. One can hence truncate Eq. (40) at  $M = M_c(\mu)$  to accurately compute the solution for the main pump tone. The result of such a study is presented in Fig. 9. We solve Eq. (40) for certain values of  $\mu$  and find the corresponding values for  $M_c$ . For  $\mu = 0.5$  we find that

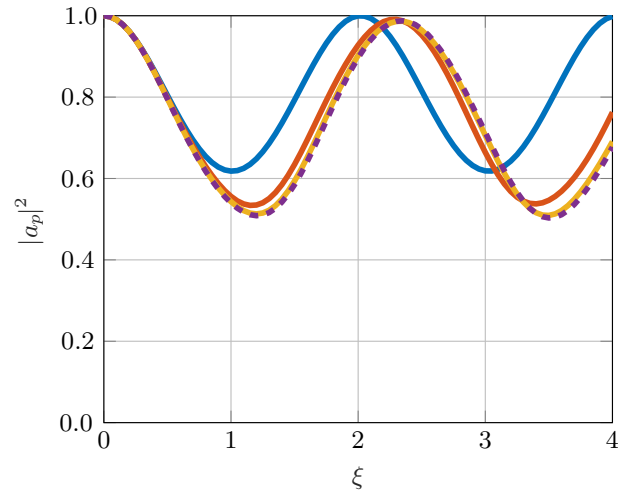


FIG. 7. Solution for  $|a_p(\xi)|^2$  to Eq. (40), using  $\mu = 2$  and a different number of harmonics included in computation,  $M = 2$  (blue), 3 (orange), 4 (yellow), 5 (dashed magenta).

$M_c = 10$ , for  $\mu = 2$  we find that  $M_c = 5$ , and for  $\mu = 8$ ,  $M_c = 3$ . Different values of  $M_c$  as a function of  $\mu$  are shown in Fig. 8. As seen in Fig. 9, the pump behavior can, in general, be summarized as follows: the pump oscillates between full transmission and some lower bound. The larger the  $\mu$ , the smaller the oscillation amplitude and period.

## B. Comparison with four-wave mixing

It is instructive to compare the pump harmonic generation studied in the previous section to the pump harmonic generation by the 4WM, where the phase mismatch introduced by the Kerr effect prevents exponential amplification. One should anticipate that a similar mechanism would

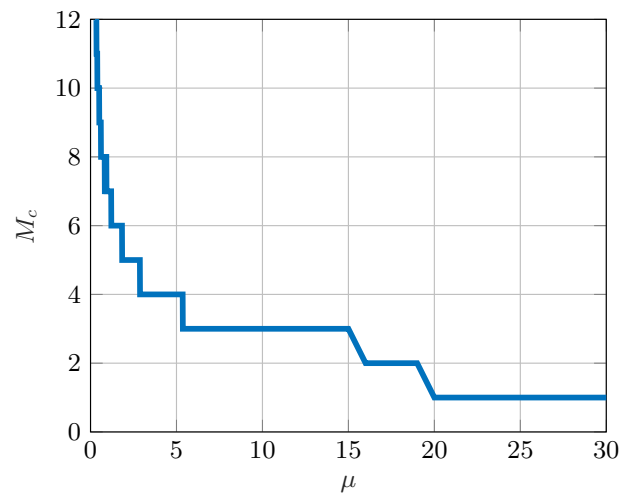


FIG. 8. The critical number of harmonics  $M_c$  for different values of  $\mu$  for the length  $\xi = 10$  and error tolerance 0.01.

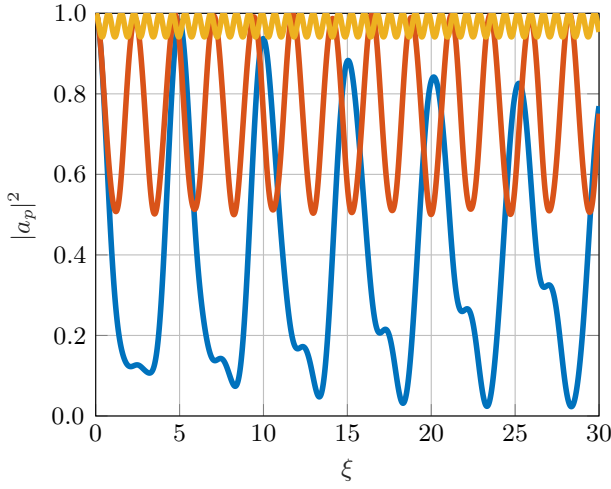


FIG. 9. Solution for  $|a_p(\xi)|^2$  to Eq. (40), using  $\mu = 0.5$  (blue), 2 (orange), and 8 (yellow) and corresponding  $M_c = 11, 6, 4$ .

suppress the generation of pump high harmonics [33]. We test this assumption by computing the third harmonic of the pump using the developed scaling method.

The equations for the pump harmonics are derived in a similar way as for the 3WM. Restricting to the third harmonic, we have,

$$A'_p = i \frac{\chi_4 a^2}{8} \left( k_p^3 A_p^2 A_p^* - k_{3p} k_p^2 A_{3p} A_p^{*2} e^{i(k_{3p} - 3k_p)x} \right), \quad (42a)$$

$$A'_{3p} = i \frac{\chi_4 a^2}{8} \left( 2k_{3p} k_p^2 A_{3p} A_p A_p^* - \frac{1}{3} k_p^3 A_p^3 e^{-i(k_{3p} - 3k_p)x} \right), \quad (42b)$$

where  $\chi_4$  is the fourth-order nonlinearity coefficient derived in a similar way to  $\chi_3$  in Sec. II. The value of  $\chi_4$  is  $\frac{1}{2}$  for a junction TWPA, while it is typically smaller for a rf SQUID or a SNAIL TWPA at zero bias. With similar rescalings as in Sec. IV A,

$$\xi = \frac{\chi_4 A_p^2(0) k_p^3 a^2}{8} x, \quad a_{mp}(\xi(x)) = m \frac{A_{mp}(x)}{A_p(0)}, \quad (43)$$

we write these equations in a dimensionless form,

$$(a_p)'_{\xi} = i \left( a_p^2 a_p^* - 3a_{3p} a_p^{*2} e^{i\mu\xi} \right), \quad (44a)$$

$$(a_{3p})'_{\xi} = 3i \left( 2a_{3p} a_p a_p^* - \frac{1}{3} a_p^3 e^{-i\mu\xi} \right). \quad (44b)$$

Here the spatial behavior of both harmonics is defined by a single scaling parameter,

$$\mu = \frac{256\Delta}{\chi_4 A_p^2(0) k_p^3 a^3} \approx \frac{8k_p^2 a^2}{\chi_4 \theta_p(0)^2}. \quad (45)$$

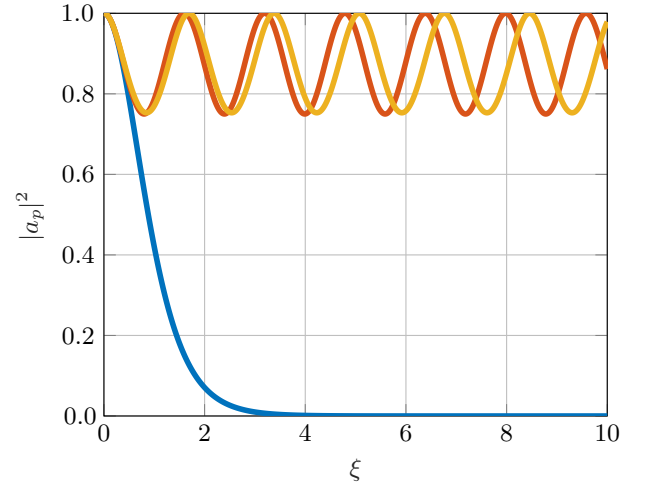


FIG. 10. Spatial dependence of pump signal under 4WM including one up-converted mode for nondispersive spectrum,  $\mu = 0$  (yellow); for comparison the pump signal under 3WM is shown for  $\mu = 0$  (blue), and for dispersive spectrum,  $\mu = 3$  (orange).

We solve Eq. (42) numerically for different values of  $\mu$ , the result is presented in Fig. 10. In contrast to 3WM, where the first harmonic is completely depleted in the absence of frequency dispersion,  $\mu = 0$  (blue line), it oscillates for the 4WM (yellow line), similar to 3WM at a considerable dispersion,  $\mu = 3$  (orange line).

Thus we conclude that the Kerr effect, caused by the  $\chi_4$  term, not only prevents exponential amplification but also suppresses the generation of higher harmonics, which makes up-conversion processes less dangerous for 4WM amplification compared to 3WM.

### C. Full multimode model

Now we proceed with the discussion of the amplification in the 3WM regime and assume a weak signal tone being injected in addition to the strong pump tone,  $A_s(0) \ll A_p(0)$ . We perform our analysis under the same assumption as in Sec. III of small amplitudes of signal and idler compared to the pump amplitude within the whole TWPA,  $A_s(x), A_i(x) \ll A_p(x)$ . This assumption allows us to neglect the back action of the signal and idler on the pump (pump depletion), and also neglect the generation of signal and idler harmonics while allowing the up-conversion of the signal and idler by the pump harmonics. The latter assumption implies a linearization of the equations with respect to all signal and idler harmonics.

With the adopted approximations, the field in the TWPA will consist of a linear combination of the pump and pump harmonics,  $m\omega_p$ , signal  $\omega_s$ , down-converted idler,  $\omega_i = \omega_p - \omega_s$ , and all their up-converted modes by the pump and pump harmonics,  $\omega_{s+mp} = \omega_s + m\omega_p$ ,  $\omega_{i+mp} =$

$\omega_i + m\omega_p$ , see Fig. 11. The ansatz is therefore,

$$\begin{aligned} \phi(x, t) = & \frac{1}{2} \sum_{m=1}^M [A_{mp} e^{ik_{mp}x - im\omega_p t} + \text{c.c.}] \\ & + \frac{1}{2} \sum_{m=0}^{M-1} [A_{s+mp} e^{ik_{s+mp}x - i(\omega_s + m\omega_p)t} \\ & + A_{i+mp} e^{ik_{i+mp}x - i(\omega_i + m\omega_p)t} + \text{c.c.}]. \end{aligned} \quad (46)$$

Using the reduced variables introduced in Eqs. (39), (41), and (27) and detuning  $\delta$  defined in Eq. (26), the equations for the signal modes take the form,

$$\begin{aligned} (a_{s+mp})'_\xi = & \left( m + \frac{1 + \delta}{2} \right) \\ & \times \left( \sum_{n=m+1}^M a_{np} a_{i+(n-m-1)p}^* e^{i\mu\xi d_{n,m}^p} \right. \\ & + \sum_{n=m+1}^{M-1} a_{s+np} a_{(n-m)p}^* e^{i\mu\xi d_{n,m}^s} \\ & \left. - \sum_{n=1}^m a_{np} a_{s+(m-n)p} e^{-i\mu\xi d_{m,(m-n)}^s} \right), \end{aligned} \quad (47)$$

where  $m \in [0, M-1]$ . The numerical factors in the exponents are derived by using the cubic approximation of the dispersion relation and have the form,

$$\begin{aligned} d_{n,m}^p = & \frac{k_{np} - k_{s+mp} - k_{i+(n-m-1)p}}{8\Delta} \\ = & \frac{1}{6} \left( n^3 - \left( m + \frac{1 + \delta}{2} \right)^3 \right. \\ & \left. - \left( n - m - 1 + \frac{1 - \delta}{2} \right)^3 \right), \\ d_{n,m}^s = & \frac{k_{s+np} - k_{s+mp} - k_{(n-m)p}}{8\Delta} \\ = & \frac{1}{6} \left( \left( n + \frac{1 + \delta}{2} \right)^3 - \left( m + \frac{1 + \delta}{2} \right)^3 - (n - m)^3 \right), \end{aligned} \quad (48)$$

where  $\Delta$  is defined in Eq. (27). The equations for the idler modes are similar, but with the replacements  $s \leftrightarrow i$  and  $\delta \leftrightarrow -\delta$ .

For  $M = 1$ , Eq. (47) reduces to the continuous analog of the three-mode model in Sec. III,

$$\begin{aligned} (a_s)'_\xi = & \frac{1 + \delta}{2} a_i^* e^{i\mu\xi(1-\delta^2)/8}, \\ (a_i)'_\xi = & \frac{1 - \delta}{2} a_s^* e^{i\mu\xi(1-\delta^2)/8}. \end{aligned} \quad (49)$$

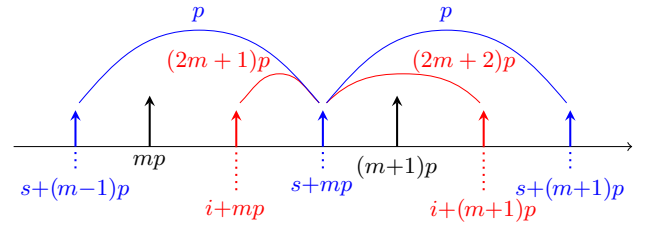


FIG. 11. Frequency diagram illustrating structure of Eq. (47) for the signal  $m$ th harmonic,  $a_{s+mp}$ ; signal modes (blue), idler modes (red), pump harmonics (black), down-conversion processes (red), and up-conversion processes (blue). Each process is marked with the pump harmonic that is driving the process.

The solution has an exponential form,  $a_s, a_i \propto e^{g\xi}$ , with the gain coefficient [10],

$$g = \frac{1}{2} \sqrt{(1 - \delta^2) \left[ 1 - \frac{\mu^2}{8^2} (1 - \delta^2) \right]}, \quad (50)$$

which coincides with the long-wave length asymptotic in Eq. (28). The exponential gain occurs only for small values of the scaling parameter given by  $\mu < 8/\sqrt{1 - \delta^2}$ .

We solve Eq. (47) numerically in the same way as we solve them for the pump harmonics, including the spatial dependence of the pump harmonics. The results for the power gain as the function of length,  $G(\xi) = |a_s(\xi)/a_s[0]|^2$ , are shown in Figs. 12 and 13 for  $\mu = 1$  and  $\mu = 10$  at zero detuning ( $\delta = 0$ ). These results demonstrate two distinctly different amplification regimes: for small values of  $\mu$ , the gain grows on average with the TWPA length, but much slower than expected from three-mode model, Eq. (50). The gain suppression is the result of the up-conversion with many up-converted modes affecting the signal. In Fig. 12, the gain reaches value  $G \sim 20$  dB at scaled length  $\xi \approx 30$ . In the opposite case of large  $\mu$ , the gain profile converges quickly, and the number of modes included in the simulation is small. Correspondingly, the gain spatial profile becomes oscillatory and has a relatively small amplitude, Fig. 13. This reduction of the gain is the effect of phase mismatch, in accord with the criterion of a nonexponential amplification of the three-mode model,  $\mu > 8$ .

While one should not expect the gain larger than few dB for TWPA with any length when  $\mu$  is large, for small  $\mu$  the gain grows with the length and interesting question is what gain can be achieved for realistic Josephson-junction TWPA. The limitation is imposed by the necessity to accommodate all relevant modes within the spectral range. For the ten pump harmonics involved, as in Fig. 12, the pump frequency should be limited,  $\omega_p < 0.1\omega_c$ , which corresponds to  $ka < 0.2$ . From Eqs. (39) and (41), we then deduce the real space length,  $x \sim 500a\xi = 15000$  unit cells. Such a long TWPA is unpractical.

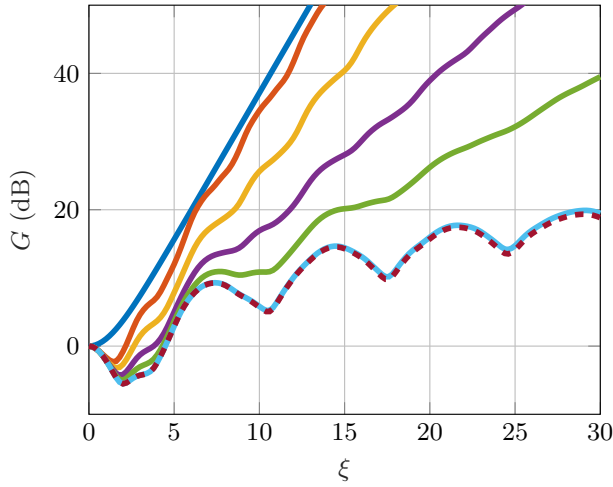


FIG. 12. Gain  $G$  for  $\mu = 1$  at zero detuning,  $\delta = 0$ , and  $M = 1, 4, 5, 6, 7$ , and  $10$  (from top to bottom), and  $M = 11$  (dashed magenta).

We compare the predicted gain by the model with simulations done with Keysight PathWave Advanced Design System (ADS) for a SNAIL-based TWPA. The simulated device consists of  $N = 440$  unit cells, each unit cell contains one junction with  $I_{c1} = 800$  nA, and  $\mathcal{N} = 3$  identical junctions with  $I_{c2} = 3$   $\mu$ A, Eq. (12). The biasing magnetic flux is applied at  $\Phi \approx 0.4\Phi_0$ , where  $\chi_3(\Phi) \approx 0.82$  [recall Eq. (15)], and the four-wave mixing vanishes. The pump frequency is placed at  $f_p = 8.5$  GHz. A comparison of the simulation results and the predicted gain by the equations is presented in Fig. 14 for two different pump currents. While the simulation in ADS has additional gain ripples that our model does not capture, the overall gain profile is very similar between the two.

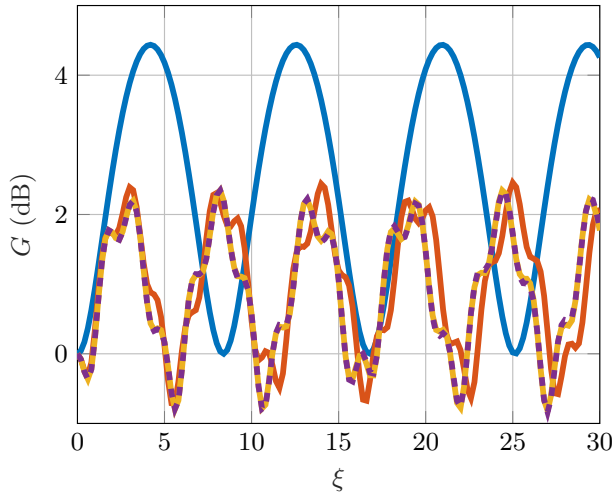


FIG. 13. Gain  $G$  for  $\mu = 10$  at zero detuning,  $\delta = 0$ , and  $M = 1$  (blue), 2 (red), 3 (yellow), and 4 (dashed purple).

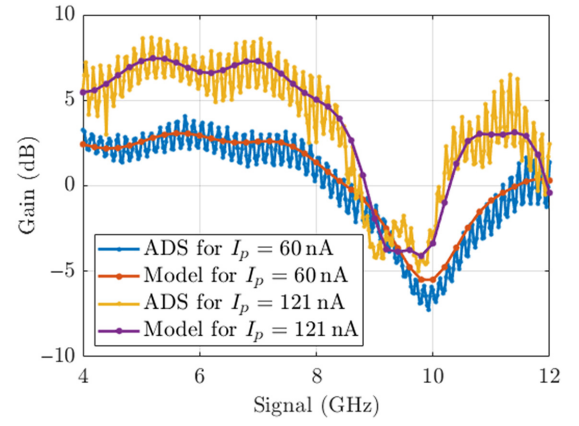


FIG. 14. Comparison between the predicted gain by our model and the predicted gain by simulations done by ADS for two different pump currents for a SNAIL-based TWPA with  $N = 440$  unit cells with  $I_{c1} = 800$  nA,  $\mathcal{N} = 3$  identical junctions with  $I_{c2} = 3$   $\mu$ A, a biasing magnetic flux  $\Phi \approx 0.4\Phi_0$  and a pump at  $f_p = 8.5$  GHz.

Summarizing, we formulate the second significant result of this paper: in the weakly dispersive spectral region of low frequencies, a gain above 20 dB is hard to achieve. For a small  $\mu$ , the gain is reduced by a strong up-conversion effect, while for a large  $\mu$ , the gain is small and oscillatory because of a large effective phase mismatch.

## V. A SOLUTION: TWO-BAND FREQUENCY SPECTRUM

In this section we revisit the three-mode model of Sec. III and consider the possibility of reducing the dispersion at high frequencies, in the no-up-conversion region,  $\omega_p > \Omega_{th} = 4\omega_0/3$ , to maintain the high gain. The idea is to create a sweet spot in the TWPA frequency spectrum where the signal injected at the degeneracy point,  $\omega_s = \omega_p/2$ , is exactly phase matched with the pump,  $\kappa_s = \kappa_p/2$ . Such a possibility does not exist for the TWPA studied in Sec. III. However, as we theoretically prove in this section, such a possibility appears for a TWPA with a two-band frequency spectrum (cf. Ref. [19]). At such a sweet spot a strong exponential amplification is predicted to occur and, moreover, it persists within a wide frequency band.

A common way to create a gap in the TWPA spectrum is to periodically modulate the device parameters along the propagation direction. This is routinely done for kinetic inductance TWPAs by modulating the geometry, and thereby the impedance, of the transmission line [13]. For the Josephson-junction TWPAs another method is used—adding linear  $LC$  oscillators to the TWPA cells. In this case, a spectral gap opens at the resonance frequency of the oscillators. This method of dispersion engineering is used in four-wave mixing devices to mitigate the Kerr effect [23–25].

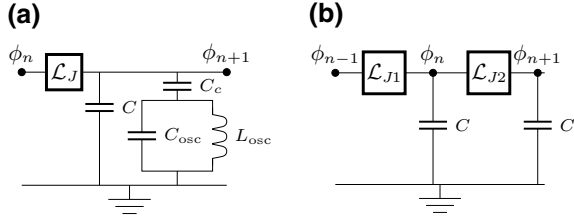


FIG. 15. Circuit diagrams for TWPA with two-band frequency spectrum; (a)  $LC$  oscillators added to the unit cells, and (b) periodically modulated parameters of the unit cells.

### A. Chain with oscillators

Let us consider the TWPA with  $LC$  oscillators. The corresponding circuit is presented in Fig. 15(a). The derivation of the dynamical equation is straightforward: we add the oscillator circuit variables to the Lagrangian, Eq. (1), and eliminate the oscillator variables from the dynamic equations. Specifically we consider the dc current-biased TWPA. In this case, Eq. (21) for the chain without oscillators remains valid with the only difference, the factor  $\omega^2/\omega_0^2$  in the first term is replaced with

$$\frac{\omega^2}{\omega_0^2} \rightarrow \frac{\omega^2 v \omega^2 - \omega_1^2}{\omega_0^2 \omega^2 - \omega_1^2}, \quad (51)$$

where

$$\omega_1^2 = \frac{1}{L_{\text{osc}}(C_{\text{osc}} + C_c)}, \quad (52)$$

$$v = 1 - \frac{C_c^2}{(C + C_c)(C_{\text{osc}} + C_c)}. \quad (53)$$

The dispersion equation then takes the form

$$4\omega_0^2 \sin^2 \frac{\kappa}{2} = \omega^2 \frac{v\omega^2 - \omega_1^2}{\omega^2 - \omega_1^2}. \quad (54)$$

Solving for  $\omega$  we get

$$\omega_{\pm}^2 = \frac{1}{2v} \left[ \left( \omega_1^2 + 4\omega_0^2 \sin^2 \frac{\kappa}{2} \right) \pm \sqrt{\left( \omega_1^2 + 4\omega_0^2 \sin^2 \frac{\kappa}{2} \right)^2 - 16v\omega_1^2 \omega_0^2 \sin^2 \frac{\kappa}{2}} \right]. \quad (55)$$

The derived spectrum is depicted in Fig. 16; it consists of two bands separated by a gap.

To identify the sweet spot we assume the pump frequency within the upper band, and the signal frequency within the lower band, and solve equation,  $\omega_-(\kappa_p/2) = \omega_+(\kappa_p)/2$ . Converted for the pump frequency, this

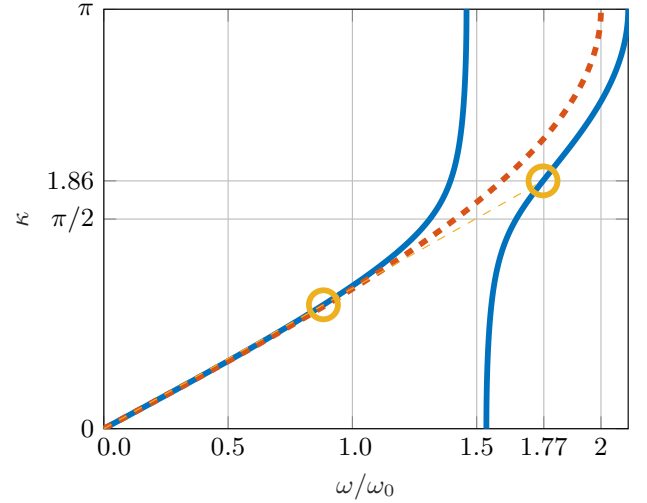


FIG. 16. Two-band frequency dispersion relation for a TWPA with  $LC$  oscillators with  $\omega_1 = 1.5\omega_0$  and  $v = 0.95$  (solid lines). The dispersion relation exhibits a frequency gap at the resonance frequency of the  $LC$  oscillator, the dashed line indicates the dispersion relation in the absence of oscillators, the circles indicate the positions of phase-matched points, which lie on a straight line within the no-up-conversion region (shown in Fig. 4).

equation has the explicit form

$$\frac{3(1-v)}{\omega_p^2 - \omega_1^2} = \frac{1}{16\omega_0^2 \omega_1^2} \frac{(4\omega_1^2 - v\omega_p^2)^2}{4\omega_1^2 - \omega_p^2}. \quad (56)$$

One can check by direct calculation that the solution indeed possesses the property,  $\kappa_s = \kappa_p/2$ , as illustrated in Fig. 16: the pump and signal points are located on a straight line. Moreover, the pump frequency is located in the no-up-conversion frequency region (recall Fig. 4).

The equations for the gain coefficient, Eqs. (28) and (29), derived in Sec. III do not change their form in the present case; however, the dependence of the gain coefficient on the frequency is now different due to the different dispersion relation. Dependence of the gain coefficient at the signal degeneracy on the pump frequency is illustrated in Fig. 17. As soon as the pump is placed within the lower frequency band, the gain coefficient behaves similarly to the one in Fig. 2(a) for a TWPA without oscillators. However, when the pump is placed within the upper band at the sweet spot, the amplification dramatically increases up to  $g \approx 0.014$  for a rather weak pumping strength,  $\varepsilon = 0.06$ , about 7 times smaller than the maximum pumping strength in Fig. 2(a) and definitely achievable in experiments. This  $g$  value corresponds to the gain  $G \approx 24$  dB for  $N = 200$  unit cells. The pump position is rather flexible, the gain remains high within the pump bandwidth approximately  $0.05\omega_0$ .

For a detuned signal, large amplification persists within a quite wide frequency band, approximately  $0.5\omega_p$  that

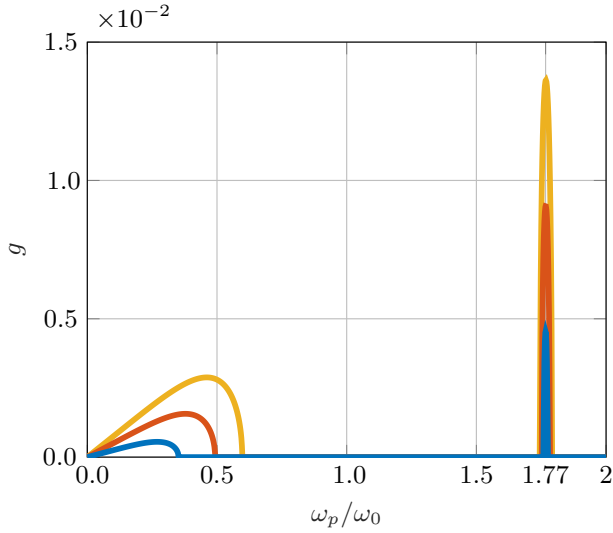


FIG. 17. Gain coefficient for a signal at zero detuning,  $\delta = 0$ , for a TWPA with a two-band dispersion relation with  $\omega_1 = 1.5\omega_0$ ,  $\nu = 0.95$  and  $\varepsilon = 0.02$  (blue), 0.04 (orange), and 0.06 (yellow). When the pump is placed within the lower band, the gain coefficient is similar to the case in the absence of oscillators (curves at the lower left corner). The sharp high-amplification peak emerges when the pump is placed within the upper band at the sweet spot,  $\omega_p = 1.77\omega_0$ . The peak widths are  $0.018\omega_0$ ,  $0.032\omega_0$ , and  $0.048\omega_0$ , respectively.

could be of the order of few GHz, as shown in Fig. 18. This is due to a relatively weak dispersion in the small frequency limit.

### B. Sweet spot in periodically modulated chain

Here we examine a periodically modulated TWPA and prove that there also exists a sweet spot. Experimental realization of such a device is reported elsewhere [35]. The circuit is presented in Fig. 15(b), here each unit cell consists of two subcells with different Josephson-junction parameters. Consider the dc current-biased TWPA with different Josephson inductances in the subcells. The Lagrangian can be written for odd and even circuit nodes in analogy with Eqs. (1) and (2),

$$\mathcal{L}_J[\theta_n] = \sum_{2n} \frac{1}{L_{J1}} \cos(\theta_{01} + \theta_{2n}) + \sum_{2n+1} \frac{1}{L_{J2}} \cos(\theta_{02} + \theta_{2n+1}). \quad (57)$$

The biasing phases here obey the equations,  $\sin \theta_{0j} = I_{dc}/I_{cj}$ . Dynamical equations for such a chain have the

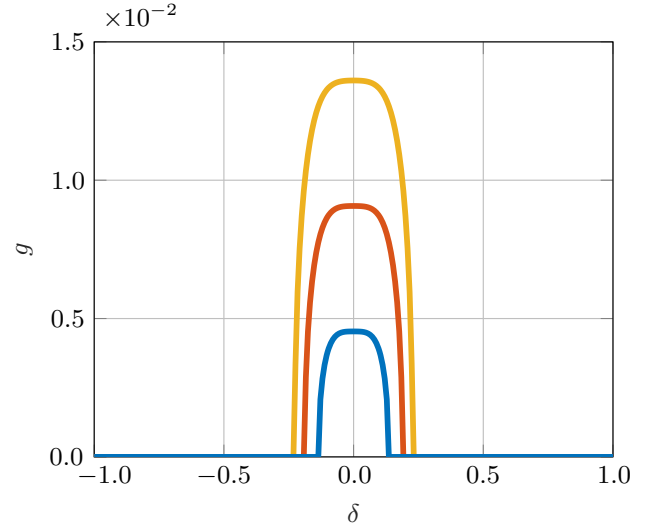


FIG. 18. Gain coefficient as a function of detuning for a TWPA with two-band dispersion relation with  $\omega_1 = 1.5\omega_0$  and  $\nu = 0.95$ , for pump at optimal phase matching point  $\approx 1.77\omega_0$  and different pumping strengths,  $\varepsilon = 0.02$  (blue), 0.04 (orange), and 0.06 (yellow). The corresponding bandwidths are  $\omega_s - \omega_p/2 = (0.14, 0.19, 0.23)\omega_p$ , respectively.

form,

$$-\ddot{\phi}_{2n} - (\omega_1^2 \theta_{2n} - \omega_2^2 \theta_{2n+1}) + \frac{1}{2} (\omega_1^2 \tan \theta_{01} \theta_{2n}^2 - \omega_2^2 \tan \theta_{02} \theta_{2n+1}^2) = 0, \quad (58)$$

$$-\ddot{\phi}_{2n+1} - (\omega_2^2 \theta_{2n+1} - \omega_1^2 \theta_{2n+2}) + \frac{1}{2} (\omega_2^2 \tan \theta_{02} \theta_{2n+1}^2 - \omega_1^2 \tan \theta_{01} \theta_{2n+2}^2) = 0, \quad (59)$$

where  $\omega_j^2 = \cos \theta_{0j} / L_J [j] C$  are the subcell resonance frequencies. The linearized equations define the spectral properties of the chain. Assume the solution having the form,  $\phi_{2n} = A e^{i\kappa(2n) - i\omega t}$ ,  $\phi_{2n+1} = B e^{i\kappa(2n+1) - i\omega t}$ , then equations for amplitudes,  $A$  and  $B$ , read,

$$(\omega^2 - \omega_1^2 - \omega_2^2)A + (\omega_1^2 e^{-i\kappa} + \omega_2^2 e^{i\kappa})B = 0, \\ (\omega^2 - \omega_2^2 - \omega_1^2)B + (\omega_2^2 e^{-i\kappa} + \omega_1^2 e^{i\kappa})A = 0, \quad (60)$$

and the dispersion relation has the form,

$$\omega^2 = (\omega_1^2 + \omega_2^2) \pm \sqrt{(\omega_1^2 + \omega_2^2)^2 - 4\omega_1^2 \omega_2^2 \sin^2 \kappa}. \quad (61)$$

The dispersion relation is depicted in Fig. 19; it has two bands separated by a gap. The sweet spot is found from

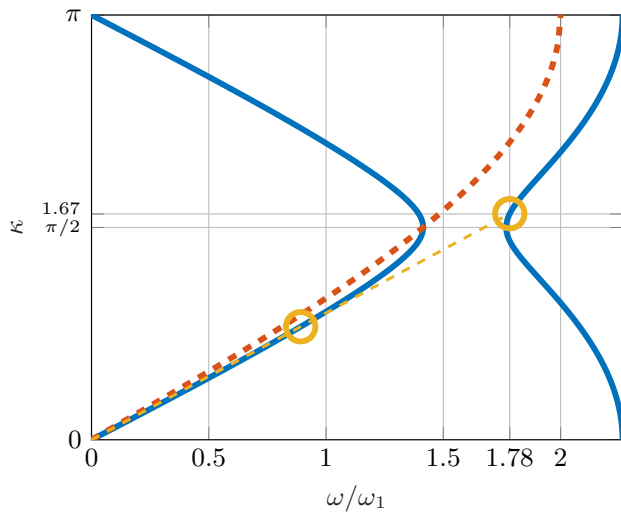


FIG. 19. Dispersion relation of a periodically modulated Josephson-junction chain with  $\omega_2 = 1.25\omega_1$ ; it consists of two bands separated by a gap (solid lines), dashed line indicates the dispersion relation in the absence of modulation, the circles indicate positions of phase-matched points, they lie on a straight line within the no-up-conversion frequency region.

equations,  $\omega_s = \omega_p/2$ ,  $\kappa_s = \kappa_p/2$ , whose solution reads,

$$\omega_p^2 = 8 \left[ (\omega_1^2 + \omega_2^2) - \sqrt{3}\omega_1\omega_2 \right], \quad (62)$$

$$\sin^2 \frac{\kappa_p}{2} = \frac{\sqrt{3} \left[ (\omega_1^2 + \omega_2^2) - \sqrt{3}\omega_1\omega_2 \right]}{\omega_1\omega_2}. \quad (63)$$

This solution is illustrated in Fig. 19: the positions of the pump and the signal at the degeneracy are indicated with the circles; they lie on a straight line at different sides of the gap in the region where the up-conversion is not possible. The gain in this setup is qualitatively similar to the TWPA with  $LC$  oscillators.

## VI. CONCLUSION

In this paper, we propose a method for achieving a high gain for a lumped-element TWPA operating in the 3WM regime. The simple model of amplification in weakly dispersive medium [9,10], relevant for kinetic inductance TWPAs and Josephson-junction TWPAs at low frequencies predicts the gain up to 40 dB for a chain with 100 unit cells and a reasonable pump intensity. However, in practice, such a gain was never demonstrated. This was explained with a parasitic effect of generation of high harmonics and up-conversion processes [34]. We perform a detailed theoretical analysis of this regime including multiple pump harmonics and signal and idler up-converted modes. We identify a scaling parameter  $\mu$  that controls

the gain and quantifies an interplay between the dispersion and the nonlinear wave interaction and find that the gain is strongly reduced for both small values as well as large values of  $\mu$ , although for different reasons. When the dispersion is weak in relation to the interaction, i.e., for small  $\mu$ , the generation of up-converted modes is prominent. In the opposite limit of strong dispersion in relation to the interaction, i.e., for large  $\mu$ , the phase mismatch becomes the dominant effect. This finding is supported by simulations done in ADS on a SNAIL TWPA, and the data is in quantitative agreement with the theoretical predictions.

Our proposal concerns a different operation regime for which the cutoff frequency of the TWPA plays the central role. We propose to place the pump close to the cutoff such that generation of up-converted modes is inhibited. Then, by solving the difference equations for discrete Josephson-junction chain we find that there is a sweet spot where the pump and the signal are exactly phase matched. The sweet spot is proven to exist when the TWPA frequency spectrum consists of two bands separated by a gap. Studying different ways of engineering the two-band spectrum—by adding  $LC$  oscillators or periodically modulating the chain parameters, we predict that the gain at the sweet spot may achieve the values of order 25 dB within a few GHz amplification bandwidth for a chain with approximately 200 unit cells and for moderate pump intensities. Such a gain is sufficient to amplify the readout signals from a few qubits within the amplifier dynamical range. To increase the dynamical range, one could modify the proposed TWPA design to increase the critical currents of the junctions together with the number of frequency bands to preserve the sweet spot position for the pump. Some reduction of the gain coefficient in this case could be compensated for by increasing the TWPA length.

## ACKNOWLEDGMENTS

The project is supported by the Knut and Alice Wallenberg foundation via the Wallenberg Centre for Quantum Technology, and the EU Consortium OpenSuperQ. The authors acknowledge the use of the Nanofabrication Laboratory (NFL) at Chalmers University of Technology.

- 
- [1] C. M. Caves, Quantum limits on noise in linear amplifiers, *Phys. Rev. D* **26**, 1817 (1982).
  - [2] T. Yamamoto, K. Inomata, M. Watanabe, K. Matsuba, T. Miyazaki, W. D. Oliver, Y. Nakamura, and J. S. Tsai, Flux-driven Josephson parametric amplifier, *Appl. Phys. Lett.*, **93**, 042510 (2008).
  - [3] N. Bergeal, F. Schackert, M. Metcalfe, R. Vijay, V. E. Manucharyan, L. Frunzio, D. E. Prober, R. J. Schoelkopf, S. M. Girvin, and M. H. Devoret, Phase-preserving amplification near the quantum limit with a Josephson ring modulator, *Nature* **465**, 64 (2010).

- [4] N. Roch, E. Flurin, F. Nguyen, P. Morfin, P. Campagne-Ibarcq, M. H. Devoret, and B. Huard, Widely Tunable, Nondegenerate Three-Wave Mixing Microwave Device Operating near the Quantum Limit, *Phys. Rev. Lett.* **108**, 147701 (2012).
- [5] A. Roy and M. Devoret, Introduction to parametric amplification of quantum signals with Josephson circuits, *Comptes Rendus Phys.* **17**, 740 (2016).
- [6] J. Aumentado, Superconducting Parametric Amplifiers (Review), *IEEE Microwave magazine*, August 2020, p. 45 (2020).
- [7] R. J. Schoelkopf and S. M. Girvin, Wiring up quantum systems, *Nature* **451**, 664 (2008).
- [8] A. L. Cullen, A travelling-wave parametric amplifier, *Nature (London)* **181**, 332 (1958).
- [9] P. K. Tien and H. Suhl, A traveling-wave ferromagnetic amplifier, *Proc. Lnst. Radio Engrs.* **46**, 700 (1958).
- [10] P. K. Tien, Parametric amplification and frequency mixing in propagating circuits, *J. Appl. Phys.* **29**, 1347 (1958).
- [11] A. L. Grimsmo and A. Blais, Squeezing and quantum state engineering with Josephson travelling wave amplifiers, *npj Quantum Inf.* **3**, 20 (2017).
- [12] M. R. Perelshstein, K. V. Petrovnin, V. Vesterinen, S. Hamedani Raja, I. Lilja, M. Will, A. Savin, S. Simbierowicz, R. N. Jabdaraghi, J. S. Lehtinen, L. Grönberg, J. Hassel, M. P. Prunnila, J. Govenius, G. S. Paraoanu, and P. J. Hakonen, Broadband Continuous-Variable Entanglement Generation Using a Kerr-Free Josephson Metamaterial, *Phys. Rev. Appl.* **18**, 024063 (2022).
- [13] Byeong Ho Eom, Peter K. Day, Henry G. LeDuc, and Jonas Zmuidzinas, A wideband, low-noise superconducting amplifier with high dynamic range, *Nat. Phys.* **8**, 623 (2012).
- [14] C. Bockstiegel, J. Gao, M. R. Vissers, M. Sandberg, S. Chaudhuri, A. Sanders, L. R. Vale, K. D. Irwin, and D. P. Pappas, Development of a broadband NbTiN traveling wave parametric amplifier for MKID readout, *J. Low Temp. Phys.* **176**, 476 (2014).
- [15] M. R. Vissers, R. P. Erickson, H.-S. Ku, Leila Vale, Xian Wu, G. C. Hilton, and D. P. Pappas, Low-noise kinetic inductance traveling-wave amplifier using three-wave mixing, *Appl. Phys. Lett.* **108**, 012601 (2016).
- [16] S. Chaudhuri, D. Li, K. D. Irwin, C. Bockstiegel, J. Hubmayr, J. N. Ullom, M. R. Vissers, and J. Gao, Broadband parametric amplifiers based on nonlinear kinetic inductance artificial transmission lines, *Appl. Phys. Lett.* **110**, 152601 (2017).
- [17] R. P. Erickson and D. P. Pappas, Theory of multiwave mixing within the superconducting kinetic-inductance traveling-wave amplifier, *Phys. Rev. B* **95**, 104506 (2017).
- [18] S. Goldstein, N. Kirsh, E. Svetitsky, Y. Zamir, O. Hachmo, C. E. Mazzotti de Oliveira, and N. Katz, Four wave-mixing in a microstrip kinetic inductance travelling wave parametric amplifier, *Appl. Phys. Lett.* **116**, 152602 (2020).
- [19] M. Malnou, M. R. Vissers, J. D. Wheeler, J. Aumentado, J. Hubmayr, J. N. Ullom, and J. Gao, Three-Wave Mixing Kinetic Inductance Traveling-Wave Amplifier with Near-Quantum-Limited Noise Performance, *PRX Quantum* **2**, 010302 (2021).
- [20] D. J. Parker, M. Savytskyi, W. Vine, A. Laucht, T. Duty, A. Morello, A. L. Grimsmo, and J. J. Pla, Degenerate Parametric Amplification via Three-Wave Mixing Using Kinetic Inductance, *Phys. Rev. Appl.* **17**, 034064 (2022).
- [21] O. Yaakobi, L. Friedland, C. Macklin, and I. Siddiqi, Parametric amplification in Josephson junction embedded transmission lines, *Phys. Rev. B* **87**, 144301 (2013).
- [22] O. Yaakobi, L. Friedland, C. Macklin, and I. Siddiqi, Erratum: Parametric amplification in Josephson junction embedded transmission lines, *Phys. Rev. B* **88**, 219904(E) (2013).
- [23] K. O'Brien, C. Macklin, I. Siddiqi., and Xiang Zhang, Resonant Phase Matching of Josephson Junction Traveling Wave Parametric Amplifiers, *Phys. Rev. Lett.* **113**, 157001 (2014).
- [24] C. Macklin, K. O'Brien, D. Hover, M. E. Schwartz, V. Bolkhovskoy, X. Zhang, W. D. Oliver, and I. Siddiqi, A near-quantum-limited Josephson traveling wave parametric amplifier, *Science* **350**, 325 (2015).
- [25] T. C. White, *et al.*, Traveling wave parametric amplifier with Josephson junctions using minimal resonator phase matching, *Appl. Phys. Lett.* **106**, 242601 (2015).
- [26] M. T. Bell and A. Samolov, Traveling-Wave Parametric Amplifier Based on a Chain of Coupled Asymmetric SQUIDS, *Phys. Rev. Appl.* **4**, 024014 (2015).
- [27] L. Planat, A. Ranadive, R. Dassonneville, J. Puertas Martínez, S. Léger, C. Naud, O. Buisson, W. Hasch-Guichard, D. M. Basko, and N. Roch, Photonic-Crystal Josephson Traveling-Wave Parametric Amplifier, *Phys. Rev. X* **10**, 021021 (2020).
- [28] A. Ranadive, M. Esposito, L. Planat, E. Bonet, C. Naud, O. Buisson, W. Guichard, and N. Roch, Kerr reversal in Josephson meta-material and traveling wave parametric amplification, *Nat. Commun.* **13**, 1737 (2022).
- [29] A. B. Zorin, Josephson Traveling-Wave Parametric Amplifier with Three-Wave Mixing, *Phys. Rev. Appl.* **6**, 034006 (2016).
- [30] A. B. Zorin, Flux-Driven Josephson Traveling-Wave Parametric Amplifier, *Phys. Rev. Appl.* **12**, 044051 (2019).
- [31] V. V. Sivak, N. E. Frattini, V. R. Joshi, A. Lingenfelter, S. Shankar, and M. H. Devoret, Kerr-Free Three-Wave Mixing in Superconducting Quantum Circuits, *Phys. Rev. Appl.* **11**, 054060 (2019).
- [32] A. Miano and O. A. Mukhanov, Symmetric traveling wave parametric amplifier, *IEEE Trans. Appl. Supercond.* **29**, 1501706 (2019).
- [33] J. A. Armstrong, N. Bloembergen, J. Ducunung, and P. S. Pershan, Interactions between light waves in a nonlinear dielectric, *Phys. Rev.* **127**, 1918 (1962).
- [34] T. Dixon, J. W. Dunstan, G. B. Long, J. M. Williams, P. J. Meeson, and C. D. Shelly, Capturing Complex Behavior in Josephson Traveling-Wave Parametric Amplifiers, *Phys. Rev. Appl.* **14**, 034058 (2020).
- [35] A. Fadavi Roudsari, D. Shiri, H. Renberg Nilsson, G. Tancredi, A. Osman, I. Svensson, M. Kudra, M. Rommel, J. Bylander, V. Shumeiko, and P. Delsing, Three-wave mixing traveling-wave parametric amplifier with periodic variation of the circuit parameters, *Appl. Phys. Lett.* **122**, 052601 (2023).

- [36] M. H. Devoret, in *Quantum Entanglement and Information Processing*, edited by D. Esteve, J. M. Raimond, and J. Dalibard, Proceedings of the Les Houches Summer School of Theoretical Physics, LXIII, 1995 (Elsevier, Amsterdam, 2004).
- [37] A. O. Caldeira and A. J. Leggett, Quantum tunnelling in a dissipative system, *Ann. Phys.* **149**, 374 (1983).
- [38] P. Hänggi, Dissipative tunneling, *Z. Phys. B* **68**, 181 (1987).
- [39] H. F. Yu, X. B. Zhu, Z. H. Peng, W. H. Cao, D. J. Cui, Ye Tian, G. H. Chen, D. N. Zheng, X. N. Jing, Li Lu, and S. P. Zhao, Quantum and classical resonant escapes of a strongly driven Josephson junction, *Phys. Rev. B* **81**, 144518 (2010).